Direct deposition of (Bi_xSb_$1-$ $-x$)_2Te_3 nanosheets on Si/SiO_2 substrates by chemical vapor transport

Felix Hansen, Rico Fucke, Titouan Charvin, Samuel Froeschke, Daniel Wolf, Romain Giraud, Joseph Dufouleur, Nico Gräßler, Bernd Büchner, Peer Schmidt, et al.

Direct deposition of $(Bi_xSb_{1-x})_2Te_3$ nanosheets on Si/SiO_2 substrates by chemical vapor transport

Felix Hansen*[1], Rico Fucke[1], Titouan Charvin[1], Samuel Froeschke[1], Daniel Wolf[1], Romain Giraud[1,4], Joseph Dufouleur[1], Bernd Büchner[1,2], Peer Schmidt[3], Silke Hampel*[1]

[1] Leibniz Institute for Solid State and Materials Research Dresden, Helmholtzstraße 20, 01069 Dresden, Germany

[2] Technische Universität Dresden, Helmholtzstr. 10, 01069, Dresden, Germany

[3] Brandenburg University of Technology Cottbus – Senftenberg, Universitätsplatz 1, 01968 Senftenberg, Germany

[4] Université Grenoble Alpes, CNRS, CEA, Grenoble-INP, Spintec, F-38000 Grenoble, France

ABSTRACT The tellurides of Bismuth and Antimony (Bi_2Te_3 and Sb_2Te_3) are prominent members of the V_2VI_3 material family that exhibit promising topological properties. We provide a method for the rational synthesis of mixed crystals of these materials ($(Bi_xSb_{1-x})_2Te_3$ with x = 0.1, ..., 0.9) by means of a bottom-up CVT approach. Thermodynamic calculations showed the synthesis to be possible in the temperature range of 390 – 560°C without significant enrichment of either component and without adding a transport agent. The starting materials were synthesized and verified by XRD. Optimization experiments showed the ideal conditions for nanosheet synthesis to be T_2 = 560°C, T_1 = 390°C with a reaction time of t = 36 h. Crystals with heights of down to 12 nm (12 quintuple layers) were synthesized and analyzed by means of scanning electron microscopy, energy-dispersive X-ray spectrometry and atomic force microscopy. High resolution transmission electron microscopy confirmed the R$\bar{3}$m crystal structure, high crystallinity and overall quality of the synthesized $(Bi_xSb_{1-x})_2Te_3$ nanosheets. Magneto-transport measurements revealed that such ternary compounds can have a significantly reduced carrier density compared to the binary parent compounds.

Introduction

In the recent years, topological insulator materials (TI) delivering promising new applications have widely grown in research interest. 3D topological insulators are generally characterized by having a fully insulating bulk band gap but have metallic surface states that are protected by time-reversal symmetry. The latter result from a symmetry inversion of the valence and conduction bands[1–4]. The V_2VI_3 material family, consisting of Bi_2Te_3, Bi_2Se_3, Sb_2Te_3 and Sb_2Se_3, is probably the most widely known family of materials that exhibit these properties with Bi_2Te_3 being its most prominent member[4,5]. V_2VI_3 materials, crystallizing in the tetradymite (Bi_2Te_2S) structure type, are layered materials with a strong anisotropy and consist of quintuple layers (QL) stacked in the order VI(1)-V-VI(2)-V-VI(1) (see Fig. 1). The stacked quintuple layers are connected by Van-der-Waals forces allowing for easy cleaving of the crystals perpendicular to the c-axis. All of the materials but Bi_2Se_3 crystallize in the R$\bar{3}$m space group[6–9].

However, it is complicated to study or use the surface state properties of these materials since a high density of charge carriers, predominantly introduced by antisite-defects or vacancies, is also present in binary compounds, thus leading to bulk conduction. In general, the Dirac point in the

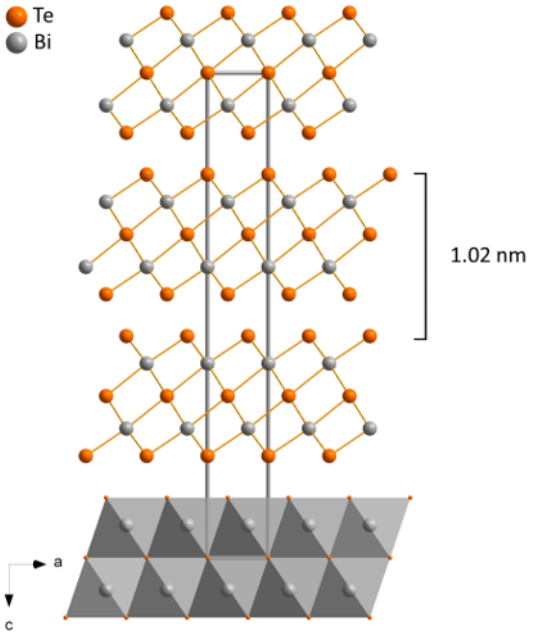

Figure 1. Layered structure of Bi_2Te_3 as an example for the V_2VI_3 material family (tetradymite structure type). The structural height of one QL accounts to 1.02 nm.

surface band structure is either well below or well above the Fermi level fixed by electrical doping. Depending on the growth method and post synthesis treatment e.g. Bi_2Te_3 can either be *n-type* or *p-type* intrinsically doped depending on a subtle balance between different point defects acting as donor or acceptors[10–13].

To make full use of the potential applications of the V_2VI_3 materials and of their nanostructures, it is necessary to develop a synthesis process that leads to minimal bulk conduction. Some non-equilibrium growth methods such as molecular beam epitaxy (MBE) or chemical vapor deposition (CVD), have already been applied in the synthesis of this material family[13–18].

In this work we focus on the bottom-up chemical vapor transport growth (more precisely: the decomposition sublimation[19]) of mixed crystal nanosheets of $(Bi_xSb_{1-x})_2Te_3$ with thicknesses < 100 nm while reaching several microns in lateral size. We aim to provide high quality mixed crystals of Bi_2Te_3 and Sb_2Te_3 with various compositions of a solid solution (x = 0.1 ... 0.9). For an ideal, yet unknown, composition the Fermi level could be shifted within the bulk band gap, due to an intrinsic charge compensation (balance of defects acting as donors or acceptors), thus reducing the conduction and therefore allowing to investigate the topological states only, as evidenced by other synthesis methods[20–22].

The CVT method allows us the bottom-up growth of the full variety of mixed nanocrystals on the surface of a Si-substrate coated with SiO_2. This growth is obtained without any catalyst deposited onto the amorphous surface. The method was shown to be successful for this purpose on other layered 2D-materials, such as Bi_2Se_3, WTe_2 or α-$RuCl_3$ before[23–25]. The CVT of bulk $(Bi_xSb_{1-x})_2Te_3$ has been described before with the use of halides as transport agent[26]. We apply a transport-agent free method for the vapor transport that was rationally planned by thermodynamic calculations using TRAGMIN to reach pristine nanosheets[27].

The highly crystalline samples on the SiO_2 surface were analyzed using scanning and transmission electron microscopy (SEM and TEM), energy dispersive X-ray spectroscopy (EDX) and atomic force microscopy (AFM) to determine the exact height of the nanosheets. Selected area electron diffraction and high-resolution-TEM were used to confirm the quality of the crystals. Additionally, basic experiments towards the transferability of the crystals and the removal of excess material by liquid exfoliation steps were performed.

Experimental

Thermodynamic calculations. For the thermodynamic calculations we used a modified version of the program package TRAGMIN[27]. All the specific thermodynamic data for all species involved is listed in the supporting information. For each simulation we used a total of $5 \cdot 10^{-5}$ mol starting materials and 10^{-9} mol Argon with a volume of the ampoule of 9.4 ml. For the simulations accounting for traces of water in the experiment (see supporting information) 10^{-8} mol H_2O were added to the system.

Synthesis. Bi_2Te_3 and Sb_2Te_3 were purchased from Alfa Aesar (USA) with purities >99.9%. The preparation steps before each sealing the ampoule were performed in a glovebox (M. BRAUN, Germany) at < 1 ppm O_2 and < 1 ppm H_2O. The $(Bi_xSb_{1-x})_2Te_3$ bulk material that was used as the starting compound in CVT was pre-synthesized. For this process, stochiometric amounts of Bi_2Te_3 and Sb_2Te_3 respective to the desired crystal composition of $(Bi_xSb_{1-x})_2Te_3$ (x = 0.1, 0.2 ... 0.9) were mixed in the glovebox (m_{total} = 1000 mg per experiment), thoroughly ground together and filled in a single chamber silica ampoule (L = 11 cm, Ø = 1 cm). The filled ampoules were evacuated and closed at <10^{-2} mbar, heated to 500°C (20 K/min) in a muffle furnace and held at that temperature for 72 h. After the furnace naturally cooled to room temperature, they were then opened inside the glovebox and samples of the products were taken for bulk XRD after grinding them up.

The products were then used for the chemical vapor transport experiments. Around 1.1 mg of the respective material were placed inside a 2-chamber-ampoule (L = 11 cm, Ø = 1 cm) alongside a 5 x 3 mm² silicon substrate coated with SiO_2 on the topside. The ampoules were sealed at <10^{-2} mbar and heated in a two-zone furnace according to the temperature regime of the respective experiment.

Optimization experiments were carried out using temperature gradients of ΔT = 50 K (T_1 = 450°C, T_2 = 500°C), ΔT = 110 K (T_1 = 420°C, T_2 = 530°C) and ΔT = 170 K (T_1 = 390°C, T_2 = 560°C), around a constant mean temperature $T_Ø$ = 475°C.

In the beginning of each experiment a reverse temperature gradient (T_1 = 550°C, T_2 = 400°C) was applied to relocate any material that was deposited on the walls of the ampoule during the preparation and sealing process back to the starting side.

Identification and characterization. After the reaction, the furnace cooled to room temperature before the ampoules were taken out and subsequently opened. Samples were analyzed using an "Axio Imager.A2m" (Carl Zeiss AG, Germany) light microscope and a "FEI Nova NanoSEM" (Thermo Fisher Scientific Inc., USA) scanning electron microscope (5 - 30 kV) with an attached "AMETEK Quanta 200/400" (AMETEK, USA) EDX (30 kV) unit with "EDXGenesis" software for quantification. The used atomic force microscope was an "icon Dimension" in tapping mode (Si single crystal tips). XRD was performed using a STADI P (STOE, Germany) device in transmission geometry with Cu source (λ = 1,5418 Å). Bright field and high-resolution TEM imaging as well SAED measurements were conducted at FEI Titan3 80-300 instrument (Thermo Fisher Scientific Inc., USA). The images were acquired using an acceleration voltage of 300 keV. For atomic resolution imaging, we employed an aberration corrector providing a resolution of up to 0.08 nm.

Results and Discussion

Modelling of the CVT process. To allow for the rational planning of the experimental approach to the synthesis, thermodynamic calculations were performed prior to the experimental efforts. The composition of the gas phase in the ampoule was calculated using the one-room-model for temperatures between 390°C and 560°C (Fig. 2). Also, the transport efficiency for all gaseous components in the system was calculated for the chemical vapor transport of $BiSbTe_3$ in the same temperature range. The standard data of $(Bi_xSb_{1-x})_2Te_3$ have been calculated based on the values of the binaries and ideal mixing entropy.

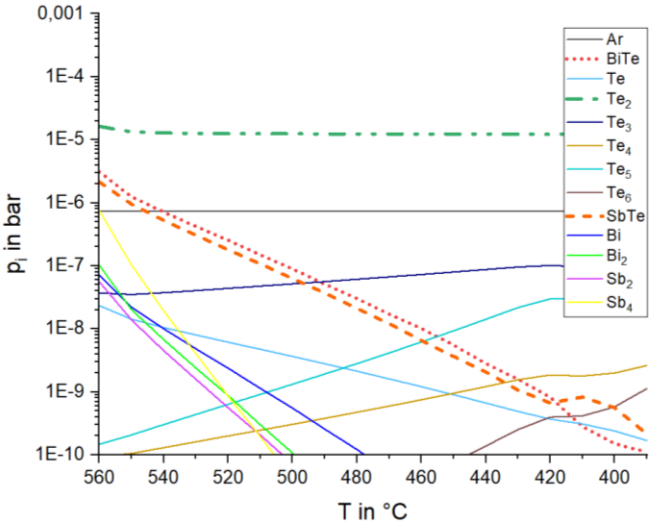

Figure 2. Composition of the gas phase over $BiSbTe_3$ (one-room-model) at different temperatures calculated using TRAGMIN[27].

No transport agent was added in the simulation.

The performed calculation of the transport process shows two main points:

(1) The partial pressure of almost all involved species is very low (see Fig. 2). For the chemical vapor transport of bulk crystals, usually species with a partial pressure below 10^{-5} bar are not taken into consideration. In this case SbTe(g) and BiTe(g) both lie around $5 \cdot 10^{-6}$ bar at the starting temperature of 560°C with a strong downwards trend. Such low partial pressure of the involved volatile species during the transport process will lead to very slow migration rates of the $(Bi_xSb_{1-x})_2Te_3$ crystals.

(2) Te_2(g) acts as the main volatile species for Tellurium, while SbTe(g) and BiTe(g) are the main volatile species for the transport of Sb and Bi respectively during the CVT. Their partial pressure p_i is at least one order of magnitude higher than every other gaseous species involving either Bi or Sb over the entire temperature range. The only exception for this is Sb_4(g) which according to the calculations can lead to a slight enrichment of antimony in the mixed crystals during the CVT. This behavior however was not measurable in the performed experiments. Apart from that, both SbTe(g) and BiTe(g) are very close to each other in their respective partial pressure over the whole temperature range of the simulation, therefore suggesting that Sb and Bi will be transported fairly congruently without any major enrichment of one or the other component in the products.

The graphs showing the transport efficiency of the single components are listed in the supporting information.

According to the calculation, the main transport reaction occurring during the CVT process (for $BiSbTe_3$ as an example) can be described as the *congruent decomposition-sublimation*:

$$BiSbTe_3(g) \rightleftharpoons BiTe(g) + SbTe(g) + \frac{1}{2}\,Te_2(g) \qquad (1)$$

The addition of traces of water to the calculations to account for realistic experimental conditions shows the emergence of several new volatile species. However, their partial pressures remain very low compared to the other species involved and therefore traces of water should not have an influence on the experiments. The result of this more extensive simulation is listed in the supporting information.

In the temperature range 560°C to 390°C there are no restrictions that prohibit the CVT of $(Bi_xSb_{1-x})_2Te_3$ crystals. Higher temperature gradients during the CVT generally lead to higher migration rates often at the cost of lower crystal quality if raised too high. However, since the migration rates in this specific system can be assumed to be very low anyway for every ΔT within the considered temperature range, a high gradient > 150 K is more appropriate to achieve the growth on a reasonable time scale for the single CVT experiments as well as influence the growth of smaller (hence thinner) crystals.

Experimental: Bulk synthesis and X-ray diffraction. Before the synthesis of the $(Bi_xSb_{1-x})_2Te_3$ nanocrystals on substrate surfaces, the starting materials for this process were pre-synthesized in bulk. The temperature for this was appointed to 500°C. After the synthesis steps, the material was then analyzed in powder XRD.

The XRD data show a progressive shift of reflexes towards higher angles with increased content of Antimony (see Fig. 3 a)) within the angular range defined by the Bragg reflections of the binary parent compounds Bi_2Te_3 and Sb_2Te_3, as expected for a solid solution. To quantify these results the data was analyzed using the software package WinXPOW to identify the lattice parameters of the structures. Theoretical values of the lattice parameters, calculated using Vegard's law, were used as starting values for the refinement.

The experimental lattice parameter *a* follows a linear trend over the whole range of x from 0.1,...,0.9 (R^2 = 0.9951) following Vegard's law (Fig. 3 b), while *c* does not follow this trend[28]. This was previously described in the literature[29].

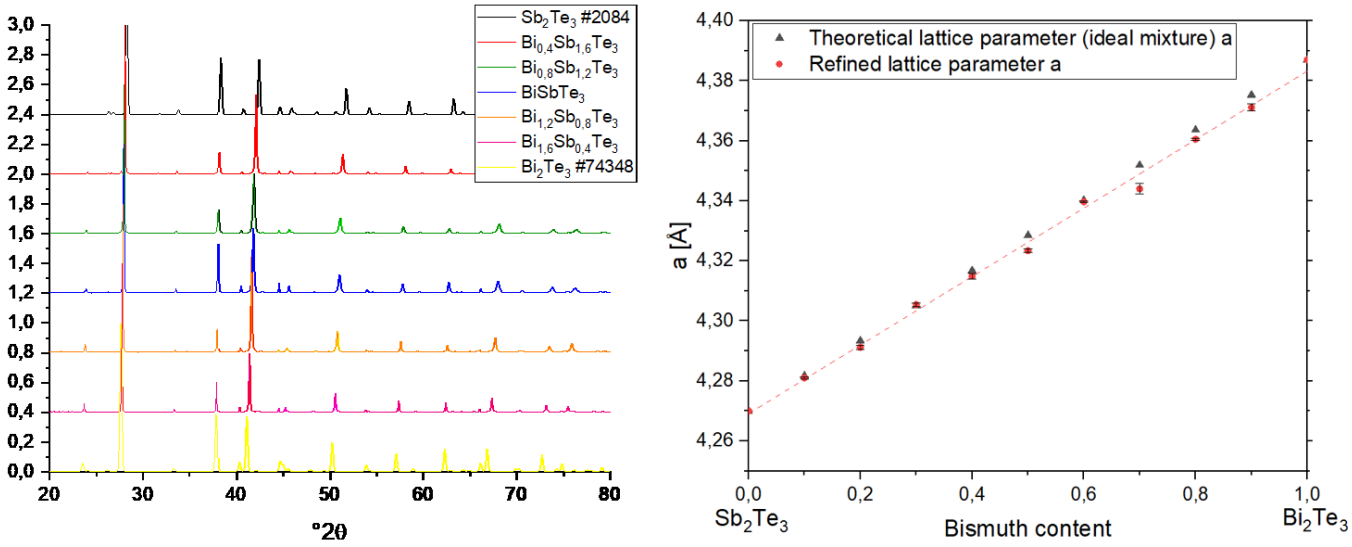

Figure 3. a) Powder X-ray diffraction patterns for $(Bi_xSb_{1-x})_2Te_3$ (x = 0, 0.2, … 0.8, 1) crystals after bulk pre-synthesis step. Shift of the reflexes towards higher angles with increasing Sb content is visible. b) Lattice parameter a vs. molar ratio x of Bi_2Te_3 shows linear trend (R^2 = 0.9951) following Vegard's law for x = 0.1,…0.9[30] . XRD for additional data points, not shown in (a) are listed in supporting information.

No additional reflexes were visible in any of the measured samples, indicating a phase pure synthesis for all values of x without any further optimization needed. Therefore, we can confirm this method to produce ideal starting materials for the further synthesis steps of the $(Bi_xSb_{1-x})_2Te_3$ nanosheets and used these in all following experiments.

Temperature gradient and reaction time. Following the rational calculation of the CVT process, as well as the synthesis of the starting materials, an optimization process was performed for the temperature gradient and the reaction time in the CVT to find the ideal conditions to synthesize $(Bi_xSb_{1-x})_2Te_3$ nanosheets. For all experiments the mean temperature was appointed to $T_{\varnothing}$ = 475°C. The optimization process was performed using $BiSbTe_3$ as the starting material and Si/SiO_2 substrates.

Using a lower temperature gradient of ΔT = 50 K (Fig. 4 a)), leads to the single crystals being larger in size. Only a few presumably thin sheets could be found in between the larger structures rendering this gradient non-optimal for our work. However, the shape of the larger crystals is pristine and for other use-cases this might very well be the optimal ΔT. With ΔT = 110 K (Fig. 4 b)), an incremental increase in the number of thinner sheets and smaller crystals in between the large structures becomes visible. This trend also applies to ΔT = 170 K (Fig. 4 c)) where a lot more of the material is deposited in small crystals, some being very thin sheets, but also irregularly shaped medium sized crystals.

Since our focus was on the $(Bi_xSb_{1-x})_2Te_3$ nanosheets which do not suffer from the irregular growth, but largely increase in numbers with increasing ΔT, we used ΔT = 170 K for any further experiments after the optimization.

For the optimization of the reaction time, we used times between t = 12 h and t = 48 h with $BiSbTe_3$ as the starting material for the synthesis. For a temperature gradient of ΔT = 170 K, after 12 h and 24 h, there is no significant growth of crystals visible on the substrate (Fig. 5 a) and b)), only very few crystals can be observed with barely any nanosheets visible. After 36 h (Fig 5 c)) large numbers of presumably thin sheets become visible on the substrate, which then vanish again when extending the reaction time to 48 h (Fig. 5 d)).

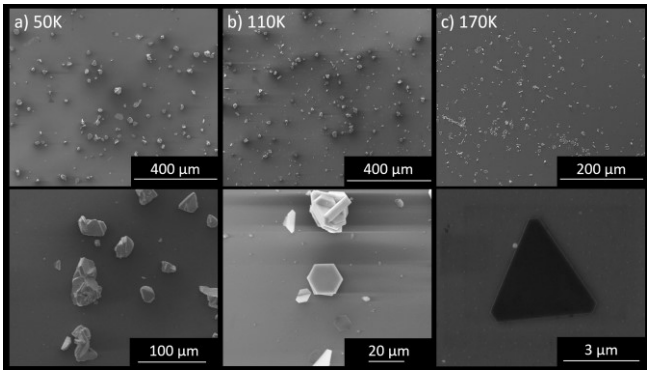

Figure 4. Comparison of SEM images of $(Bi_xSb_{1-x})_2Te_3$ (x = 0.5) microstructures grown on Si/SiO_2 substrates at different temperature gradients. $T_{\varnothing}$ = 475°C, t = 36h. a) T_2 = 500°C, T_1 = 450°C; large crystals and agglomerates, almost no thin sheets, low nucleation rate b) T_2 = 530°C, T_1 = 420°C; moderate nucleation rate, medium sized crystals, some thin sheets visible between crystals, c) T_2 = 560°C, T_1 = 390°C; high nucleation rate, moderate sized crystals (some with non-regular shape), highest number of thin sheets, as visible in bottom image

This trend is visible for all CVT processes we performed in this work. The maximum number of crystals on the substrate is reached after an optimum reaction time, after which the number of crystals starts to decrease again.

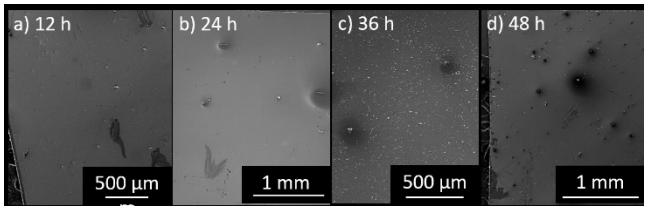

Figure 5. Comparison of SEM images of $(Bi_xSb_{1-x})_2Te_3$ (x = 0.5) microstructures grown on Si/SiO_2 substrates at different reaction times. T_2 = 560°C, T_1 = 390°C. a) t = 12 h; no significant growth of crystals observable b) t = 24 h; still very little growth c) t = 36 h; maximum number of visible crystals, many thin sheets; d) t = 48 h; almost all crystals vanish, a few still remain on the substrate.

There is no evidence that the remaining crystals on the substrate grow in size at the same time, making it unlikely that the smaller crystals decompose as part of Ostwald ripening. Rather, a second transport process is happening inside the ampoule. Due to the geometry of the ampoule it's impossible to place the substrate at the very end of the tip. This leads to a second, much smaller temperature gradient between the substrate and the very tip of the ampoule as its coldest point. Even when the material predominantly crystalizes on top of the substrate, after enough time it gets transported off the substrate again and deposits at the coldest point of the ampoule. Even though the reaction time to reach maximum number of crystals varies with the temperature gradient, this decomposition effect after maximum growth is visible for all performed optimization experiments as seen from microscopic images (Fig. 6).

The optimum synthesis conditions for $(Bi_xSb_{1-x})_2Te_3$ (x = 0.5) nanosheets were finally found to be ΔT = 170 K with $T_{\emptyset}$ = 475°C and a reaction time of t = 36 h. These conditions were used for any further experiments.

Variation of composition. After optimizing the CVT process for $BiSbTe_3$ we used the same conditions to synthesize a full variation of $(Bi_xSb_{1-x})_2Te_3$ crystals (x = 0, 0.1, 0.2 ... 1). SEM alongside Energy dispersive X-ray spectroscopy was used to analyze the synthesized mixed crystals. EDX shows a good accordance between the theoretical values of Bi content and the measured values (Fig. 7 a)) for all synthesized compounds. All displayed EDX values are averages of three different crystals on the substrate surface of each respective sample. Small deviations from the ideal values are within the margin of error for the method. Due to overlapping of the relevant Sb and Te peaks in the EDX, using the Bi content is the most reliable method of quantifying the results.

Thin sheets presumably down to the nanoscale are clearly present for all compositions, as shown in Fig. 7 b), c) and d), with a subjectively larger amount of them with increasing Bi content. Generally, crystal growth is very alike over the entire range of x, with as much variation of the growth behavior in the reproduction of single samples, as between different samples of the series. Crystals have either triangular or hexagonal shapes with a prevalence of trigonal crystals for the nanosheets. Larger crystals form agglomerates and partly grow in irregular shapes as previously mentioned. There is a distinct difference in the contrast behavior of the as grown crystals on the substrate surface in the SEM images. While most of the crystals that seem three dimensional are much brighter than their background, for some crystals this contrast seems to even out (Fig. 7 c)) or even invert with distinctly darker nanostructures than the background (Fig. 7 b) and d)). As this goes along with a weaker visible edge effect as well as a generally worse visibility especially with higher acceleration voltages (> 10 keV) it is very likely that this indicates especially thin sheets.

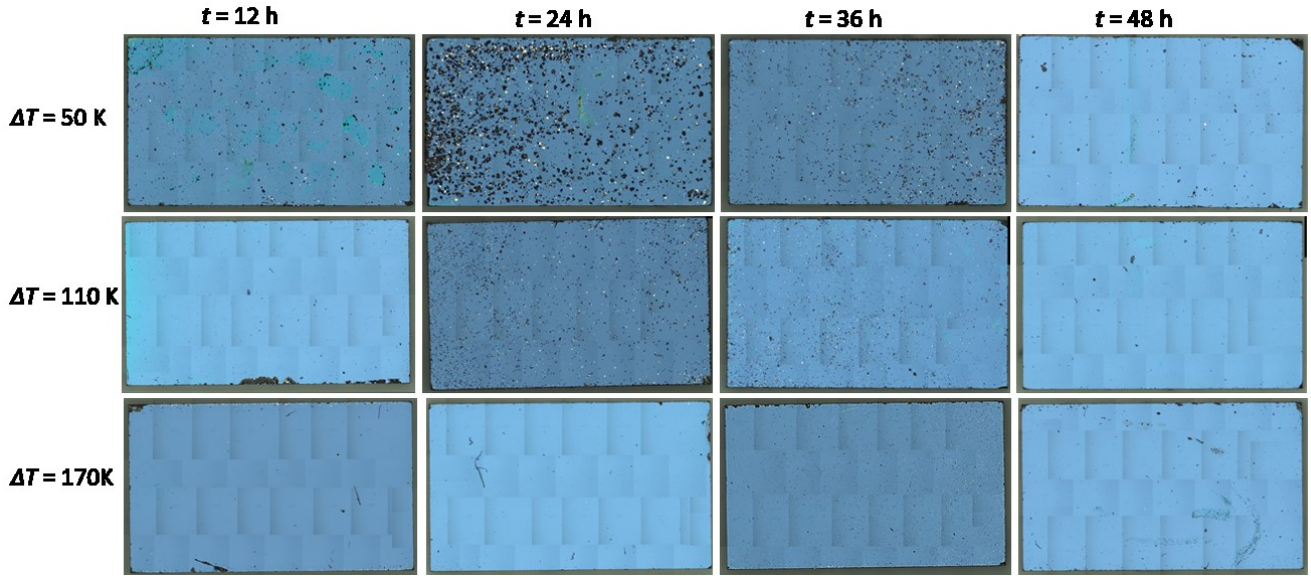

Figure 6. Comparison of light microscope images (full substrate; 3 x 5 mm²) of the optimization process of nanosheet growth for $(Bi_xSb_{1-x})_2Te_3$ (x = 0.5). The maximum number of crystals is reached after 24 or 36h respectively for the different ΔT and decreases subsequently indicating a second transport effect in the ampoule during synthesis.

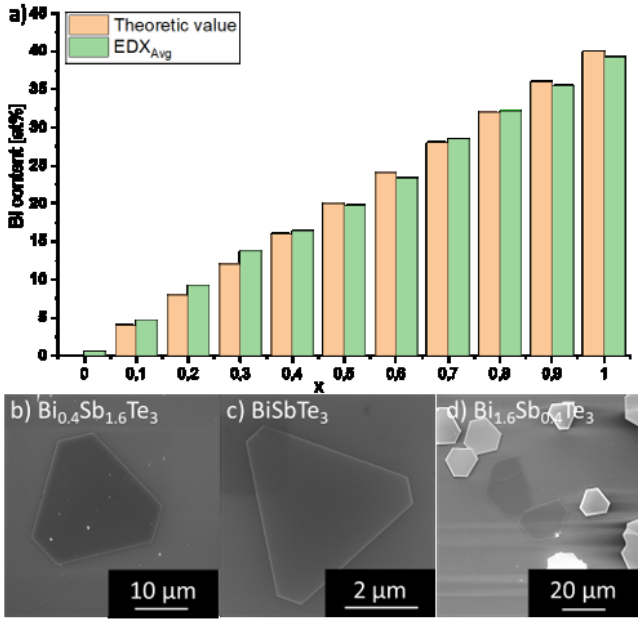

Figure 7. EDX data and SEM images of multiple samples of $(Bi_xSb_{1-x})_2Te_3$. a) EDX for $(Bi_xSb_{1-x})_2Te_3$ (x = 0, 0.1, … 1) compared to theoretical values; b) and c) SEM images of as grown nanosheets of $Bi_{0.4}Sb_{1.6}Te_3$ and $BiSbTe_3$ respectively; d) direct comparison of nanosheets in the center vs. thicker crystals of $Bi_{1.6}Sb_{0.4}Te_3$ in SEM

It is explained by primary electrons penetrating through the thin crystals while the lower energy secondary electrons that re-exit the substrate underneath are then blocked partly by the thin crystal sheet on top. This explains a direct link between the thickness of the crystals and the inversion of the contrast in SEM.

Using both electron microscopy and optical microscopy, we were able to define different sets of crystals with comparable optical properties for a given group, so as to then specifically target these and further analyze them using atomic force microscopy (AFM).

Atomic force microscopy. After promising crystals for further analysis were chosen, their positions on the substrates were marked and the crystals were analyzed using atomic force microscopy to evaluate their exact height. Tapping mode was used to record complete profile scans of the respective samples.

In all of the compositions x = 0.1…0.9 nanosheets (< 50 nm) were present and could be investigated by AFM. While the majority of the crystals is thicker and most of the thin crystals are in the range of 50 – 100 nm, crystals as thin as h = 12 nm (see Fig. 8) were present on several substrates. This corresponds to around 12 quintuple layers of the respective material, based on a Van-der-Waals height of around 1 nm (10 Å) per layer.

Generally, a higher number of thinner sheets with more pristine crystal appearance were found with increasing Bi-content of the respective sample. Yet, since only 10 - 15 crystals per substrate were analyzed using AFM, this trend heavily depends on the pre-choice of crystals in light microscopy and SEM.

AFM analysis proves the successful synthesis of nanosheets with heights < 50 nm for all samples with lateral dimensions of several microns. Thus, the bottom-up synthesis of these homogenous mixed crystals is successful down to at least 10 nm.

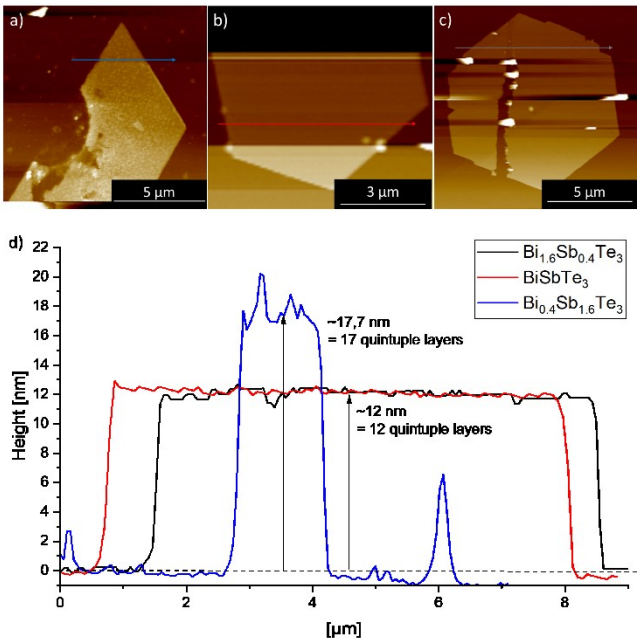

Figure 8. AFM of several samples of different compositions. a) $Bi_{0.4}Sb_{1.6}Te_3$ crystal with a non-ideally grown center, h = 17.7 nm; b) nanosheet of $BiSbTe_3$, h = 12 nm; c) $Bi_{1.6}Sb_{0.4}Te_3$, h = 12 nm; with mechanical post-synthesis damage; d) Height measurements of crystals a) – c).

Transmission electron microscopy. To verify the R$\bar{3}$m crystal structure of the synthesized nanosheets, aberration corrected high resolution transmission electron microscopy (HR-TEM) and selected area electron diffraction (SAED) were performed. Samples were prepared on lacey carbon supported TEM copper grids.

For the preparation, substrates with grown $Bi_{1.6}Sb_{0.4}Te_3$ crystals were soaked with small amounts (1 – 2 ml) of *N*-Methyl-2-pyrrolidon (NMP) and subsequently put in an ultrasonic bath for 4 – 5 min. 10 µl of the liquid were then poured on the surface of the copper grid and dried off by slight warmth from underneath (50°C in ~ 1 cm distance). This application procedure was repeated 20 times on the same grid. While it was not possible to maintain the original trigonal or hexagonal shape of the crystals (see Fig. 9 a)), we were able to transfer a sufficient amount of material on the grid to allow for a sophisticated analysis of the structure of the particles. For the fitting, a modified .cif-file was used, with the lattice parameters appointed according to the theoretical values for $Bi_{1.6}Sb_{0.4}Te_3$.

The high crystallinity of the material is clearly visible in the HR-TEM images (Fig. 9 b)) by the resolved atomic columns. Lattice planes (110) and ($\bar{1}$1$\bar{5}$) and the corresponding crystal orientation [$\bar{5}$52] were determined by this electron micrograph. The orientation is also supported by selected

area electron diffraction as shown in Fig 9 d). While the SAED diffraction pattern (Fig. 9 d)) shows a Laue diagram, supporting a high single-crystallinity over a larger region of microns, the Fourier transform of the precisely calibrated HR-TEM image (Fig. 9 c) was used for comparison with a simulated SAED pattern based on the .cif, as shown in Fig. 9 e).

Using HR-TEM and SAED, the structures synthesized on the surface of the substrates were verified to be $Bi_{1.6}Sb_{0.4}Te_3$ crystallized in the R$\bar{3}$m space group with nearly perfect agreement with the simulation for an ideal mixed crystal.

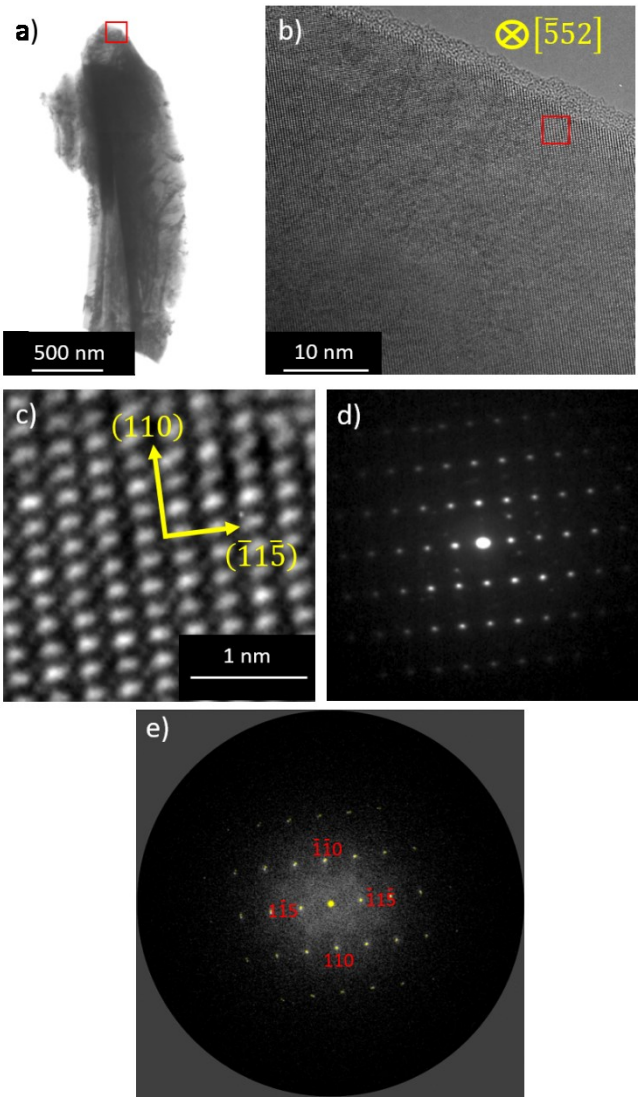

Figure 9. TEM analysis on an individual $Bi_{1.6}Sb_{0.4}Te_3$ nanoflake. a) Bright-field TEM image of the nanoflake closely analyzed in b) – e); b) High-resolution TEM image in [$\bar{5}$5$\bar{2}$] orientation of the region indicated by the red square in (a) showing the atomic structure; c) Zoom-in marked by red square in b) allowing identification of the crystal lattice planes; d) SAED pattern of top part of crystal shown in a) indicating high single crystallinity; e) Overlay view of simulated diffraction pattern (yellow dots) and Fourier transform of HR-TEM image revealing nearly perfect match.

Growth statistic and removal of excess material. Using a combination of optical microscopy, SEM and AFM, we were able to define several thickness categories for flakes, subsequently allowing us to estimate the thickness of a flake just by the appearance of the flake in optical microscopy.

As a purely optical classification, this is prone to a level of uncertainty.

We defined an area of 400 x 400 µm² on a substrate with as-grown $Bi_{1.6}Sb_{0.4}Te_3$ crystals. This area was then used as a baseline before the sample was treated in 5 ml NMP in an ultrasonic bath for 30 s. After drying off the substrate, the counting was repeated. This process was repeated 3 times for a total of 90 s in an ultrasonic bath.

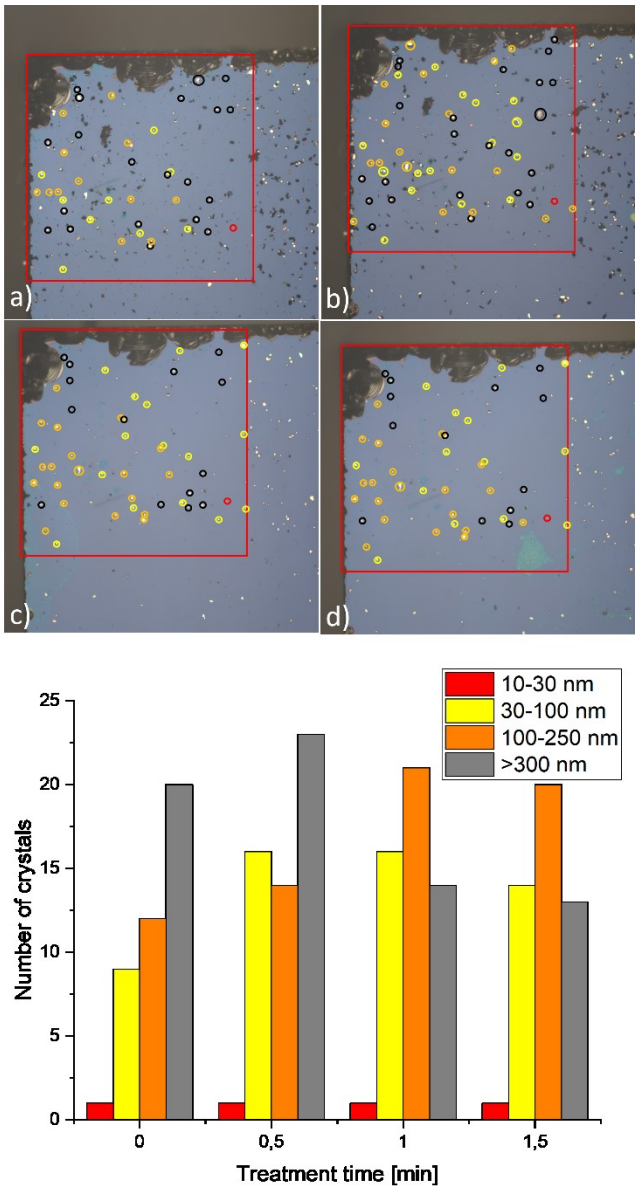

Figure 10. Light microscopic images of substrates with grown $Bi_{1.6}Sb_{0.4}Te_3$. The flat (white) crystals within the marked 400 x 400 µm² area are marked and categorized by height. a) no treatment, baseline; b) t = 30 s; c) t = 60 s, almost all of the excess material removed; d) t = 90 s; no further improvement. e) Statistical overview, crystals grown out of plane (visibly black) are not counted due to strong agglomeration.

The area before any treatment is shown in Fig. 10 a). Most of all three-dimensional crystals are grown on top visible as black structures. Most of the thinner sheets are also well visible alongside one very thin nanosheet (shown and analyzed before in Fig. 8 c)). Only a small number of crystals is thin or very thin, while all the three-dimensional crystals and sheets > 200 nm can be considered excess material. While 30 s of treatment do not have a major impact (Fig. 10 b), it is visible that most of the three-dimensional material was successfully removed after 1 min (Fig. 10 c)). Also, a high amount of the thicker sheets was removed. A longer treatment time of 1:30 min (Fig. 10 d)) shows only a minor further improvement over 1 min.

Magneto-transport properties. The bulk carrier density and mobility in $(Bi_xSb_{1-x})_2Te_3$ nanostructures were inferred from magneto-transport measurements performed on individual nanostructures patterned as a Hall bar. Our samples show a dirty metal-like behavior in the temperature dependence of the resistivity, as seen in Fig.11 for a $BiSbTe_3$ nanostructure with a rather small residual resistance ratio R300K/R4K of about 2.9, a typical value for disordered 3D topological insulators. The average carrier density is about $1.8{\cdot}10^{19}$ cm^{-3}, as inferred from the Hall resistance measured at 2K, a significantly lower value than the carrier density of thin films [31].

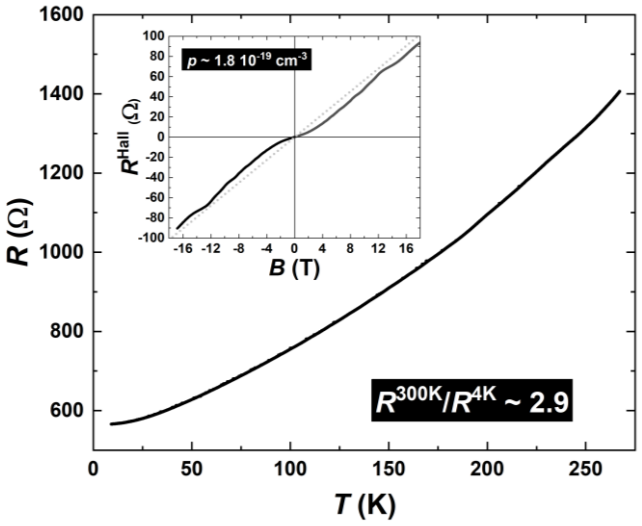

Figure 11. Temperature dependence of the resistance of a 60 nm thick $BiSbTe_3$ nanostructure, patterned as a Hall bar. Inset: Magnetic-field dependence of the Hall resistance, as measured at T = 2 K by applying the field perpendicular to the sample plane.

Conclusions

In this work, we successfully evaluated the transport agent free CVT process for Bi_2Te_3, Sb_2Te_3 and their respective mixed crystals rationally, by a thermodynamic approach. The congruent decomposition sublimation reaction was verified to be possible in the temperature range of 390°C – 560°C by sophisticated thermodynamic modelling and the main involved gas species were identified as BiTe(g), SbTe(g) and Te_2(g).

The starting materials for the CVT process were synthesized by combining Bi_2Te_3 and Sb_2Te_3 in an evacuated ampoule in their respective stochiometric amount and heat them to 500°C for 72 h. The produced starting materials were evaluated by powder XRD and shown to be phase pure. With raised Bi-content, the lattice parameter *a* increases linearly, following Vegard's law, as previously described in the literature[29,30].

Subsequent optimization for the synthesis process to produce the maximum number of nanosheets on the Si/SiO_2 substrate surface was carried out and results were evaluated by means of optical microscopy and electron microscopy. The ideal conditions were found to be T_2 = 560°C, T_1 = 390°C with a reaction time of t = 36 h. With these conditions the full series of mixed crystals of $(Bi_xSb_{(1-x)})_2Te_3$ was successfully synthesized and evaluated by SEM, EDX and subsequent AFM analysis of promising structures. All measured crystal compositions fit the projected theoretical values with a small margin of error and sheets < 50 nm in height were observable in all samples with several crystals being as thin as 12 nm (12 quintuple layers).

Samples of $Bi_{1.6}Sb_{0.4}Te_3$ were then analyzed by atomic resolution TEM and SAED and the results were successfully fitted with the theoretic values for an ideal mixed crystal of the aforementioned composition.

Additionally, we showed that the removal of excess material and crystals not grown in the correct orientation towards the substrate surface could be removed by ultrasonic treatment for 1-2 min in a small amount of solvent (NMP) without removing or destroying the nanosheets.

We therefore conclude that this bottom-up method is suitable for the controlled and rational synthesis of $(Bi_xSb_{(1-x)})_2Te_3$ nanosheets on Si/SiO_2. Magneto-transport measurements revealed the reduced bulk carrier density in such ternary com-pound nanostructures, by about one order of magnitude with respect to the case of binary compound nanostructures.

With future research it may be possible to control the synthesis more exactly and tune the dimensions of the nanosheets to the requirements of their respective use-case. The provided crystals will allow for more detailed research on the topological properties of the V_2VI_3 family that will be carried out in a future work.

ASSOCIATED CONTENT

Supporting Information:

- Thermodynamic data for modeling
- More extensive modeling results (transport efficiencies and modeling with water traces)

AUTHOR INFORMATION

Corresponding Author

Felix Hansen – f.hansen@ifw-dresden.de

Silke Hampel – s.hampel@ifw-dresden.de

Author Contributions

The manuscript was written through contributions of all authors. All authors have given approval to the final version of the manuscript.

ACKNOWLEDGMENT

The authors gratefully thank Robert Heider for the experimental help.

ABBREVIATIONS

AFM – Atomic Force Microscopy
CVT – Chemical Vapor Transport
HR-TEM – High-Resolution Transmission Electron Microscopy
NMP – *N*-Methyl-2-pyrrolidone
SAED – Selected Area Electron Diffraction
SEM – Scanning Electron Microscopy
TEM – Transmission Electron Microscopy

REFERENCES

1. Qi, X. L. & Zhang, S. C. Topological insulators and superconductors. *Rev. Mod. Phys.* **83**, (2011).
2. Chuang, P. Y. *et al.*, Anti-site defect effect on the electronic structure of a Bi_2Te_3 topological insulator. *RSC Adv.* **8**, 423–428 (2018).
3. Moore, J. E. The birth of topological insulators. *Nature* **464**, 194–198 (2010).
4. Zhang, H., Liu, C. X., Qi, X. L., Dai, X., Fang, Z. & Zhang, S. C. Topological insulators in Bi_2Se_3, Bi_2Te_3 and Sb_2Te_3 with a single Dirac cone on the surface. *Nat. Phys.* **5**, 438–442 (2009).
5. Chen, Y. L., Analytis, J. G., Chu, J. H., Liu, Z. K., Mo, S. K., Qi, X. L., Zhang, H. J., Lu, P. H., Dai, X., Fang, Z., Zhang, S. C., Fisher, I. R., Hussain, Z. & Shen, Z. X. Experimental realization of a three-dimensional topological insulator, Bi_2Te_3. *Science (80-.).* **325**, 178–181 (2009).
6. Akshay, V. R., Suneesh, M. V. & Vasundhara, M. Tailoring Thermoelectric Properties through Structure and Morphology in Chemically Synthesized n-Type Bismuth Telluride Nanostructures. *Inorg. Chem.* **56**, 6264–6274 (2017).
7. Nakajima, S. The crystal structure of $Bi_2Te_{3-x}Se_x$. *J. Phys. Chem. Solids* **24**, 479–485 (1963).
8. Tideswell, N. W., Kruse, F. H. & McCullough, J. D. The crystal structure of antimony selenide, Sb_2Se_3. *Acta Crystallogr.* **10**, (1957).
9. Mansour, A. N., Wong-Ng, W., Huang, Q., Tang, W., Thompson, A. & Sharp, J. Structural characterization of Bi_2Te_3 and Sb_2Te_3 as a function of temperature using neutron powder diffraction and extended X-ray absorption fine structure techniques. *J. Appl. Phys.* **116**, (2014).
10. Cho, S., Kim, Y., Divenere, A., Wong, G. K., Ketterson, J. B., Meyer, J. R., Cho, S., Kim, Y., Divenere, A., Wong, G. K., Ketterson, J. B. & Meyer, J. R. Antisite defects of Bi_2Te_3 thin films. *Appl. Phys. Lett.* **75**, (1999).
11. Oh, M. W., Son, J. H., Kim, B. S., Park, S. D., Min, B. K. & Lee, H. W. Antisite defects in n-type $Bi_2(Te,Se)_3$: Experimental and theoretical studies. *J. Appl. Phys.* **115**, 1–5 (2014).
12. Miller, G. R. & Li, C. Y. Evidence for the existence of antistructure defects in bismuth telluride by density measurements. *J. Phys. Chem. Solids* **26**, 173–177 (1965).
13. Dannangoda, G. C., Key, C., Sumets, M. & Martirosyan, K. S. Transition of p- to n-Type Conductivity in Mechanically Activated Bismuth Telluride. *J. Electron. Mater.* **47**, 5800–5809 (2018).
14. Del Frari, D., Diliberto, S., Stein, N., Boulanger, C. & Lecuire, J. M. Comparative study of the electrochemical preparation of Bi_2Te_3, Sb_2Te_3, and $(Bi_xSb_{1-x})_2Te_3$ films. *Thin Solid Films* **483**, 44–49 (2005).
15. Lee, C. W., Kim, G. H., Kang, S. G., Kang, M. A., An, K. S., Kim, H. & Lee, Y. K. Growth behavior of Bi_2Te_3 and Sb_2Te_3 thin films on graphene substrate grown by plasma-enhanced chemical vapor deposition. *Phys. Status Solidi - Rapid Res. Lett.* **11**, 2–5 (2017).
16. Lu, W., Ding, Y., Chen, Y., Wang, Z. L. & Fang, J. Bismuth telluride hexagonal nanoplatelets and their two-step epitaxial growth. *J. Am. Chem. Soc.* **127**, 10112–10116 (2005).
17. Aabdin, Z., Peranio, N., Winkler, M., Bessas, D., König, J., Hermann, R. P., Böttner, H. & Eibl, O. Sb_2Te_3 and Bi_2Te_3 thin films grown by room-temperature MBE. *J. Electron. Mater.* **41**, 1493–1497 (2012).
18. Liu, X., Smith, D. J., Fan, J., Zhang, Y. H., Cao, H., Chen, Y. P., Kirby, B. J., Sun, N., Ruggiero, S. T., Leiner, J., Pimpinella, R. E., Hagmann, J., Tivakornsasithorn, K., Dobrowolska, M. & Furdyna, J. K. Topological insulators Bi_2Te_3 and Bi_2Se_3 grown by MBE on (001) GaAs substrates. *AIP Conf. Proc.* **1416**, 105–108 (2011).
19. Oppermann, H., Schmidt, M. & Schmidt, P. Autotransport oder Selbsttransport - Systeme mit Gasphasentransporten unter dem eigenen Zersetzungsdruck. *Z. Anorg. Allg. Chem.* **631**, 197–238 (2005).
20. Zhang, J., Chang, C.-Z., Zhang, Z., Wen, J., Feng, X., Li, K., Liu, M., He, K., Wang, L., Chen, X., Xue, Q.-K., Ma, X. & Wang, Y. Band structure engineering in $(Bi_{1-x}Sb_x)_2Te_3$ ternary topological insulators. *Nat. Commun.* **2**, 574 (2011).
21. Kong, D., Chen, Y., Cha, J. J., Zhang, Q., Analytis, J. G., Lai, K., Liu, Z., Hong, S. S., Koski, K. J., Mo, S.-K., Hussain, Z., Fisher, I. R., Shen, Z.-X. & Cui, Y. Ambipolar field effect in the ternary topological insulator $(Bi_xSb_{1-x})_2Te_3$ by composition tuning. *Nat. Nanotechnol.* **6**, 705–709 (2011).
22. Liu, W., Endicott, L., Stoica, V. A., Chi, H., Clarke, R. & Uher, C. High-quality ultra-flat $BiSbTe_3$ films grown by MBE. *J. Cryst. Growth* **410**, 23–29 (2015).
23. Grönke, M., Schmidt, P., Valldor, M., Oswald, S., Wolf, D., Lubk, A., Büchner, B. & Hampel, S. Chemical vapor growth and delamination of α-$RuCl_3$ nanosheets down to the monolayer limit. *Nanoscale* **10**, 19014–19022 (2018).
24. Nowka, C., Veyrat, L., Gorantla, S., Steiner, U., Eichler, B., Schmidt, O. G., Funke, H., Dufouleur, J., Büchner, B., Giraud, R. & Hampel, S. Catalyst-free Growth of Single Crystalline Bi_2Se_3 Nanostructures for Quantum Transport Studies. *Cryst. Growth Des.* **15**, 4272–4278 (2015).
25. Hansen, F., Wels, M., Froeschke, S., Popov, A., Wolf, D., Büchner, B., Schmidt, P. & Hampel, S. Thermodynamic Evaluation and Chemical Vapor Transport of Few-Layer WTe_2. *Cryst. Growth Des.* **20**, 7341–7349 (2020).
26. Schöneich, M., Schmidt, M. P. & Schmidt, P. Chemical vapour transport of bismuth and antimony chalcogenides M_2Q_3 (M = Sb, Bi, Q = Se, Te). *Zeitschrift fur Anorg. und Allg. Chemie* **636**, 1810–1816 (2010).
27. Krabbes, G., Bieger, K.Sommer, H., Söhnel, T. & Steiner, U. GMIN 5.1: Package TRAGMIN for calculations of thermodynamic equilibrium. (2014).
28. Vegard, L. Die Konstitution der Mischkristalle und die Raumfüllung der Atome. *Zeitschrift für Phys.* **5**, 17–26 (1921).
29. Abrikosov, N. K., Bankina, V. F., Poretskaya, L. V., Shelimova, L. E. & Skudnova, E. V. Semiconducting II–VI, IV–VI, and V–VI Compounds. in *Semiconducting II–VI, IV–VI, and V–VI Compounds* (1969). doi:10.1007/978-1-4899-6373-4.
30. Vegard, L. Die Konstitution der Mischkristalle und die Raumfüllung der Atome. *Z. Phys.* **5**, 17–26 (1921).

31. Murmu, P. P., Kennedy, J., Suman, S., Chong, S. V., Leveneur, J., Storey, J., Rubanov, S. & Ramanath, G. Multifold improvement of thermoelectric power factor by tuning bismuth and antimony in nanostructured n-type bismuth antimony telluride thin films. *Mater. Des.* **163**, 107549 (2019).